

Nonuniform Receding Dynamics of Thin Viscous Oil Films on Roughened Surfaces

Jiatong Jiang, Suparit Tangparitkul, Mark C. T. Wilson,* and David Harbottle*



Cite This: *Energy Fuels* 2024, 38, 16114–16124



Read Online

ACCESS |



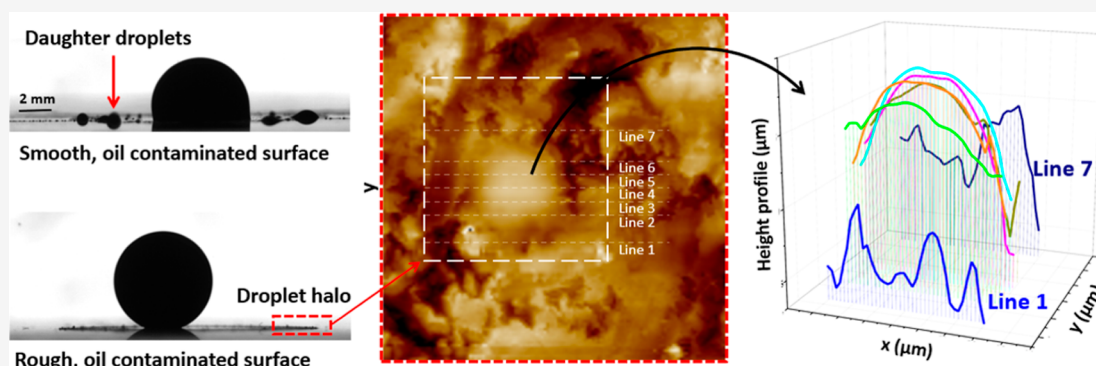
Metrics & More



Article Recommendations



Supporting Information



ABSTRACT: Liquids in contact with chemically and physically heterogeneous surfaces are ubiquitously encountered, yet little is understood about how those surface heterogeneities affect the dewetting dynamics of thin liquid films. Variations in the local contact line mobility cause nonuniform dewetting, and our working hypothesis was to decouple those heterogeneities to explain the role of each on the local contact line mobility of a viscous liquid. Thin liquid film recession was measured on roughened surfaces that were either clean or contaminated by clustered macromolecules. Atomic force microscopy was used to characterize the surface features (peaks and troughs) before and after droplet dewetting. Surfaces were initially wetted by the highly viscous liquid in air before flooding with water. On roughened uncontaminated surfaces, a pattern of smaller micron-sized droplets dispersed around the receded primary droplet remained on the surface. On chemically contaminated surfaces those micron-sized droplets were only seen on the roughest surfaces, and on smoother surfaces, secondary daughter droplets were formed but were much larger and less in number. The larger droplets formed due to the chemical heterogeneity. The smaller micron-sized droplets formed due to variations in the local contact line velocity which occurred at surface pits due to the changing apparent contact angle. Hence, the size of daughter droplets corresponded to the size of the surface pits. For roughened surfaces, the effect of chemical heterogeneity was less significant than the physical roughness which had more of an influence on modulating the local mobility of the receding contact line.

1. INTRODUCTION

Droplet-surface interactions and the associated dynamics are critical to the performance of numerous processes, for example self-cleaning surfaces,^{1,2} the recovery of crude oil^{3–5} and inkjet printing.⁶ Many interesting phenomena can be observed when liquids interact with solid surfaces, and by understanding the governing scientific principles of those interactions, it is then possible to manipulate them to produce fascinating behaviors/features such as patterned surfaces,^{7,8} enhanced mixing of droplets,^{9,10} accelerated wetting dynamics,¹¹ and many more.

Dewetting is the process of a liquid reducing its contact area on a surface, and the driving force for droplet recession is governed by the balance of interfacial energies between the three contacting phases. Droplet dewetting on uniform surfaces is well described but is more complex and less well understood on surfaces that include both chemical and physical heterogeneities. For smooth surfaces with chemical heterogeneity, we have shown that highly viscous oil droplets

undergo discontinuous dewetting which leads to the formation of small daughter droplets.¹² Those smaller droplets form due to the uneven motions of the local contact line, with the contact line moving slower on hydrophobic patches than the hydrophilic substrate. Droplet separation can also occur on uniform surfaces. Podgorski et al.¹³ observed the dynamics of a droplet running down an inclined smooth plate due to gravity and showed that the shape of the moving droplet was independent of the droplet size and depended only on the capillary number (Ca). The shape of the droplet changed from

Received: June 7, 2024

Revised: July 30, 2024

Accepted: August 7, 2024

Published: August 26, 2024



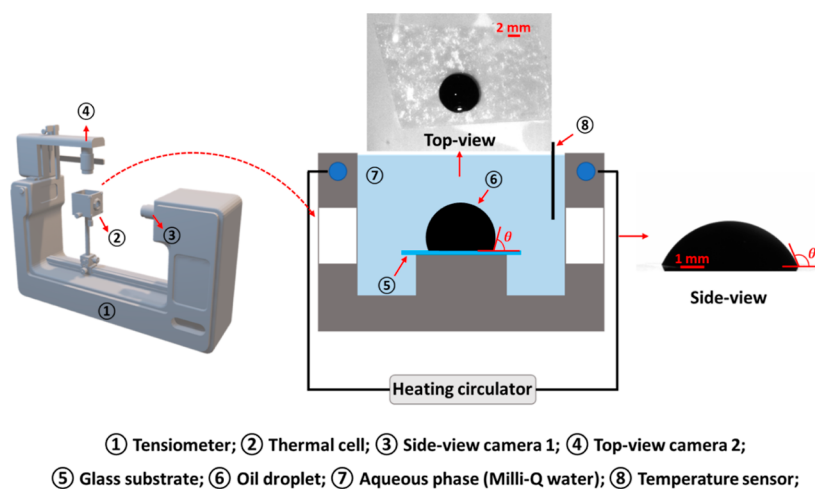


Figure 1. Schematic of the experimental setup used to observe the dewetting processes of viscous oil films. It is noted that the contact angle (θ) is measured through the aqueous phase and not the droplet. This is to maintain convention with the Young's theory.

a rounded drop to a pearling drop with increasing Ca , in order to keep the velocity constant within the fluid, and finally, pearling drop and small daughter droplets were formed above a critical Ca .

For surfaces that are chemically homogeneous but rough, the equilibrium contact angle is described by a modified contact angle, known as the Wenzel contact angle, where water-wet surfaces appear more hydrophilic when roughened, and oil-wet surfaces more hydrophobic.^{14–16} The condition for Wenzel wetting is met when a rough surface is fully wetted by the liquid droplet.¹⁷ While the Wenzel angle describes the equilibrium-state, the effect of the surface roughness induced wetted-state on the droplet dewetting dynamics is rarely studied. Using grid-patterned surfaces, Hu et al.¹⁸ observed the spreading of water droplets immersed in viscous oils that Wenzel-wetted the surface. As the water droplet advanced across the surface, small oil droplets were formed in the grid cavities. The authors attributed the formation of oil droplets to the cavity dimension, showing through a simple geometry calculation that when s/h (where s is cavity length and h the pillar height) is less than $\tan \theta_A$ (advancing contact angle), small oil droplets remain.

For chemically heterogeneous surfaces, the equilibrium contact angle is described by the Cassie model, $\cos \theta_c = f \cos \theta_{y1} + (1 - f) \cos \theta_{y2}$, where f is the fractional surface area of component 1, and θ_{y1} and θ_{y2} are the Young's contact angles on both components.^{19,20} While the equilibrium-state is understood, droplet dynamics on such surfaces are less so. Using hydrophilic–superhydrophobic patterned surfaces, Chang et al.²¹ studied the mobility of water droplets on Cassie-wetted surfaces. Dragging the droplet over the patterned surfaces the authors observed preferential wetting on hydrophilic patches, with small daughter droplets formed on those patches. The authors stated that daughter droplets form because of a pinning force, $F = L\gamma (\cos \theta_r - \cos \theta_a)$, where L is the pinning width, γ is the water–gas interfacial tension and $\theta_{a/r}$ are the advancing/receding contact angles.

The Cassie–Baxter model describes heterogeneous surfaces that are roughened (porous, pillared), with the heterogeneity resulting from an inability of the droplet to wet into the pores. The equilibrium contact angle is described by the Cassie–Baxter angle, $\cos \theta_{CB} = f(\cos \theta_y + 1) - 1$.^{22,23} Droplet

dynamics on Cassie–Baxter surfaces can vary with changes in surface topology even though f is constant.²⁴ Jiang et al.²⁵ studied water droplets advancing and receding on pillared and porous surfaces. For the same f , the advancing and receding contact angles differed between the pillared and porous surfaces, with the relative contributions from the liquid–solid and liquid–gas interfacial energies changing. This led to different pinning forces, and for the same f (0.13), the authors observed droplet separation as a water droplet receded on the pillared surface but not on the porous surface.

A transition from an apparent Cassie–Baxter state to the stable Wenzel state is often seen for liquid droplets that are deposited on roughened surfaces in air.^{26,27} Murakami and co-workers studied this wetting transition for water droplets deposited on pillar-patterned hydrophobic surfaces.²⁸ Vertical penetration of the water into grooves on the textured surfaces occurred when the interfacial energy of the Wenzel state ($E_W = \left(1 + \frac{\pi h}{2\sqrt{3}x}\right)\gamma_{SL}$, where $\frac{h}{x}$ is the substrate aspect ratio, γ_{SL} is the solid–liquid interfacial tension) was lower than that of the Cassie–Baxter state ($E_{CB} = f\gamma_{SL} + (1 - f)\gamma_{LG} + \left(1 + \frac{\pi h}{2\sqrt{3}x} - f\right)\gamma_{SG}$, where f is the corresponding fractional liquid/solid interface, γ_{LG} and γ_{SG} are the liquid–gas and solid–gas surface tensions, respectively).

The current study considers the spontaneous dewetting of highly viscous oil films on smooth and roughened surfaces that are either pristine and hydrophilic, or chemically contaminated and hydrophobic. While much effort is given to understanding thin oil film dewetting on roughened chemically contaminated surfaces, reference is also made to our previous study¹² where we evaluated the dewetting of viscous oil films on smooth chemically heterogeneous surfaces. The latter is needed to provide a comprehensive assessment of the two factors, chemical and physical heterogeneities, each of which influence dewetting dynamics. The objective is to better understand the critical role of each heterogeneity, chemical and physical, on the droplet dewetting dynamics. Most real surfaces exhibit both heterogeneities and to determine the effect of each they must be mutually studied.

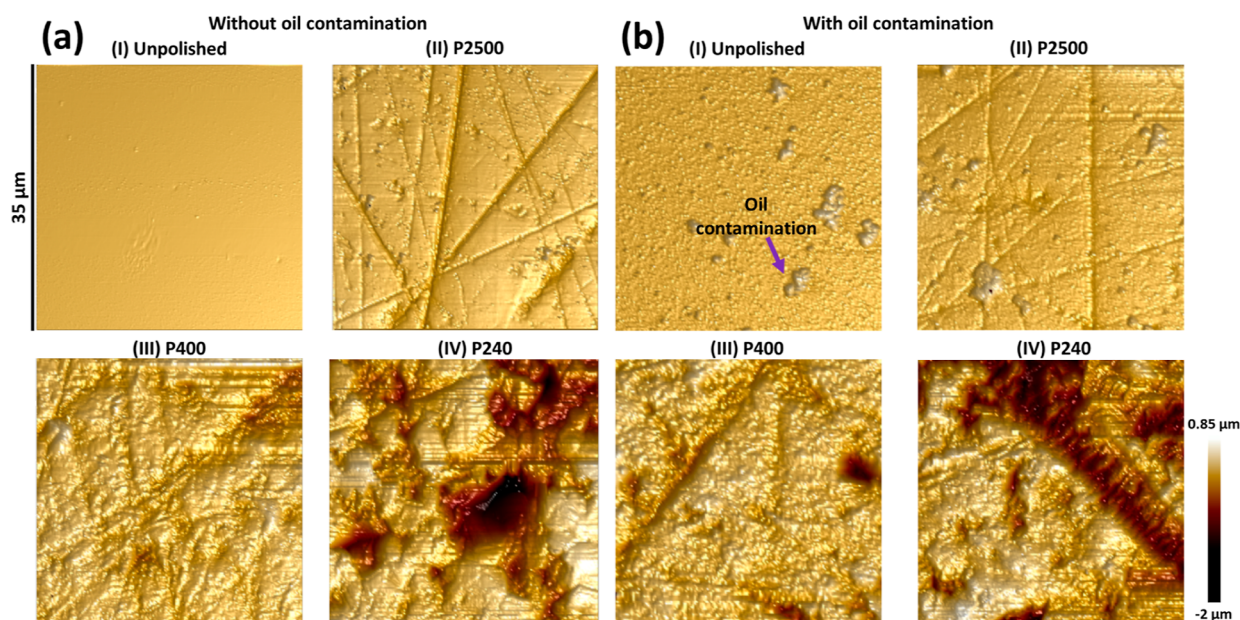


Figure 2. Surface topologies characterized by AFM tapping mode of (a) water-wet clean glass surfaces and (b) oil contaminated surfaces with different roughness. I, II, III, IV represent unpolished surface, surface polished by sandpapers with grits of P2500, P400 and P240, respectively.

2. MATERIALS AND METHODS

For all tests a Colombian heavy crude oil was used which had a fluid viscosity of 0.4 Pa s at 60 °C. Other physical properties of the oil are provided in our previous publication.¹² Milli-Q water (Merck Millipore, USA) with a resistivity of 18.2 MΩ-cm was used as the aqueous phase at pH 5.5 ± 0.5. Two solvents, toluene and *n*-heptane (Fisher Scientific, UK) had a purity of >99% and were used without further purification.

2.1. Substrate Preparation. The test substrates were borosilicate glass (>80% SiO₂, Fisher Scientific, UK). The glass slides were cleaned with excess Milli-Q water, dried with a gentle flow of nitrogen gas, and exposed to UV/Ozone (Procleaner, Bioforce Nanosciences, USA) for 20 min to remove any residual organics before storing the surfaces in a desiccator prior to use. All test substrates were prepared fresh and used the same day to minimize contamination by dust and other organics.

A grinder-polisher (Ecomet 250, Buehler, Germany) operating for 10 min at 150 rpm and with an applied force of 25 N was used to roughen the glass slides. Three sandpapers of various grit size (P240, P400 and P2500) were used to generate surfaces of different roughness. After polishing, the roughened surfaces were sonicated in 2% Decon solution for 10 min, before following the same surface cleaning procedure previously described.

Test substrates were either pristine (uncontaminated surfaces) or contaminated by soaking them for 24 h in 5 g/L heavy crude oil in Heptol 1:1 (heptane/toluene, 1:1 vol/vol). The contaminated surfaces were washed with Heptol 1:1 to remove any loosely bound deposits, before drying the glass slides in a fume hood for 24 h. The solvent Heptol 1:1 was used as it is below the asphaltene precipitation limit, hence the deposits formed are comparatively smoother than the physical roughening of the surfaces.

2.2. Oil Droplet Dewetting. We have previously studied the effect of temperature on the droplet dewetting rate, showing that the rate of dewetting corresponds to the viscosity of the heavy oil which depends on the system temperature.^{29,30} Based on our previous findings we selected 60 ± 1 °C as the test temperature since it provides optimal dynamics for data capture. A 10 ± 1 μL oil droplet was deposited onto the test substrate using an Eppendorf pipette. The test fluid was preheated to 80 °C to lower its viscosity so that a small volume droplet could be deposited. Once deposited on the surface the droplet spread to its steady-state, with the temperature of the droplet then equilibrated to the environment, 60 °C.

The experimental setup is shown in Figure 1. After the oil droplet had spread, Milli-Q water at 60 °C was gently poured into the test cell to fully submerge the oil film. As the water interface rose beyond the test substrate, the oil film began to recede and this process was captured at 2 fps using two cameras, see Figure 1. To keep convention with the Young's theory, the contact angle is measured through the aqueous phase, such that for contact angles <90° the surface is hydrophilic and for contact angles >90° the surface is hydrophobic. Further details about determining the initial condition and subsequent image processing is provided in our previous publication.¹² Each experiment was repeated with the data provided in Figure S3 of the Supporting Information.

The experimental dimensionless parameters (Bo, Re, We and Ca) are discussed in Section S1 of the Supporting Information. The basis for the calculation is for a droplet dewetting on an unmodified (unpolished and no contamination) hydrophilic glass substrate, since the contact line mobility on roughened surfaces cannot be accurately measured. As such, those values are an approximation of those for the roughened and contaminated surfaces.

2.3. Receding Contact Angle. The receding contact angle of a heavy crude oil droplet on the different test surfaces was measured by withdrawing the heavy crude oil at a constant rate using a 22-gauge hooked-needle (C210-22, Hamilton, Switzerland), see Figure S1a of the Supporting Information. To do this, the heavy crude oil droplet had to be first deposited on the test substrate, and this was done following the method previously described. The hooked needle was submerged into preheated ($T = 60$ °C) Milli-Q water in the test cell and heavy crude oil was dispensed from the needle at 0.1 μL/s until the droplet volume was 1 μL. The test substrate with the deposited oil droplet was then inverted and gently submerged in the Milli-Q water. This caused the oil droplet to recede to its new equilibrium-state, and once stable, the oil droplet on the hooked needle was aligned to the receded oil droplet and slowly moved into contact to coalesce the two droplets. The oil droplet was then withdrawn at a rate of 0.1 μL/s (Figure 1b). All images were processed using the instrument software (OneAttention), and the receding angle was taken as the average of the left and right contact angles. All experiments were conducted at 60 ± 1 °C and repeated at least 3 times.

2.4. Topographical Imaging. The test substrates were imaged at two length scales using atomic force microscopy (AFM) and confocal laser scanning microscopy (CLSM). A detailed explanation on the methods is provided in our previous publication.¹² In brief, multiple

locations on the test surfaces were scanned over an area of $35 \mu\text{m}^2$ using an Innova AFM (Bruker) operated in tapping mode with an amplitude set point of 0.6 V. All measurements were carried out at ambient conditions. A monolithic silicon cantilever (Tap300AI-G, Budget Sensors) with a force constant of $\sim 40 \text{ N/m}$ and resonance frequency of 300 kHz was used for imaging. The cantilever tip had a radius of 10 nm and so any distortion of the line profile due to tip shape is considered to be negligible.³¹ For image processing, all images were flattened using a first-order polynomial, before

determining the areal root-mean-square roughness ($R_{\text{q-AFM}} = \sqrt{\frac{\sum Z_i^2}{n}}$, where n is the number of sampled points in a frame of 256×256 scan lines and Z_i is the height at point i). For the CLSM measurements, larger scans (3.3 mm^2) were made, see Figure S2 of the Supporting Information, and the $R_{\text{q-CLSM}}$ values determined following the standard image processing method.

2.5. Numerical Simulations. To complement the experimental observations and illustrate dewetting dynamics near localized topographical features, numerical simulations were conducted using the lattice Boltzmann method. The in-house code used in our previous dewetting study was extended to include 3D topographies representing surface roughness.¹² Since the oil droplet is very large compared to the length scale of the roughness, the droplet was modeled as a segment of an infinitely long liquid bead aligned along the z axis direction, with periodic conditions applied at each end. A lattice of $151 \times 85 \times 101$ nodes (in x , y and z directions respectively) was used, with dewetting occurring in the negative x direction, and y representing the vertical direction. The topographical features of interest here are pits in the surface. These were created by first assigning the bottom 20 layers of nodes to be solid, then creating a focal pit with a specific size, shape and position by assigning nodes within the pit to be fluid nodes. Finally, smaller surface pits of random size were positioned randomly over the whole solid surface to create a rough surface.

The fluid and phase interaction parameters were the same as in our previous study¹² and further details of the underpinning multiphase model can be found in ref 32. Note that since the solid surface is now rather complex, the geometric boundary condition used previously for controlling the contact angle is difficult to implement. Instead, the wettability of the solid surface is here determined by specifying an artificial fluid density $\rho_s = \rho_w + \eta(\rho_o - \rho_w)$ on the solid surface, where ρ_o and ρ_w are the densities associated with the oil and water phases respectively, and $\eta \in [0,1]$ is a normalized “wetting parameter”.³³ Setting $\eta = 0$ corresponds to a steady-state contact angle $\theta = 0$ (measured through the aqueous phase) and $\eta = 1$ corresponds to $\theta = 180^\circ$. Since the purpose of the simulations here is to explore the effect of topography independently of chemical heterogeneity, the same value of η was specified over the whole solid surface.

3. RESULTS AND DISCUSSION

3.1. Surface Characterization. All surfaces without and with oil contamination were characterized using AFM, see Figure 2. As seen in Figure 2a, the surface is increasingly roughened when using sandpaper of a larger grit size. Using the AFM, each surface was imaged over an area of $35 \mu\text{m}^2$ and the surface roughness (R_{q}) was found to increase from $0.009 \mu\text{m}$ ($\pm 0.1\%$) to $0.301 \mu\text{m}$ ($\pm 1.5\%$) from the unpolished to P240 surfaces, respectively (Table 1). Following oil contamination, clustered deposits of different sizes were seen on the smoother surfaces [Figure 2b(I,II)], with those deposits less easily identified on the rougher surfaces, possibly because they are similar in size to that of the surface asperities. Those clustered deposits were previously shown to be asphaltenes,¹² which is reasonable since the heavy crude oil has a very high asphaltene content, $\sim 39.5 \text{ wt } \%$ as measured by the SARA analysis method.⁵

Table 1. Roughness Characteristics of the Four Surfaces with and without Oil Contamination

	surface without oil contamination		oil contaminated surface	
	$R_{\text{q-AFM}}$ (μm)	roughness ratio (r) ^a	$R_{\text{q-AFM}}$ (μm)	r
unpolished	0.009 ($\pm 0.1\%$)	1.001 ($\pm 0.1\%$)	0.011 ($\pm 0.1\%$)	1.012 ($\pm 0.2\%$)
P2500	0.048 ($\pm 0.5\%$)	1.008 ($\pm 0.4\%$)	0.042 ($\pm 0.7\%$)	1.023 ($\pm 1.7\%$)
P400	0.098 ($\pm 0.9\%$)	1.026 ($\pm 1.3\%$)	0.146 ($\pm 0.8\%$)	1.060 ($\pm 1.0\%$)
P240	0.301 ($\pm 1.5\%$)	1.076 ($\pm 4.5\%$)	0.356 ($\pm 5.5\%$)	1.137 ($\pm 6.5\%$)

^a $a_r = \frac{\text{total surface area}}{\text{projected surface area}}$.

For oil-contaminated surfaces the measured R_{q} values were higher than those of the untreated surfaces, confirming the deposition of clustered asphaltenes on all surfaces. The same approach was also used to measure R_{q} values over a larger scan area (3.3 mm^2) using the CLSM (Figure S2). The general trends agreed with the AFM analysis, although the R_{q} values tended to be higher than those measured by AFM, with those differences more apparent for the oil contaminated surfaces. While the two techniques show consistent trends, the R_{q} values by AFM have been used to further interpret the droplet dynamics on the different substrates, see discussions below. These values were used since AFM provides a direct measure of surface roughness (via contact mode imaging), rather than the noncontact method of CLSM.

3.2. Droplet Dewetting on Smooth and Roughened Surfaces (without Oil Contamination). Measuring the oil droplet contact angle on the uncontaminated surface, the change in the Gibbs free energy ($\frac{\Delta G}{\Delta A} = -\sigma_{\text{OW}} \cos \theta$) as the system moves from solid–oil–air to solid–oil–water is calculated to be -11 mN/m , confirming the heavy crude oil film spontaneously dewets when immersed in Milli-Q water. The dewetted steady-state of the heavy crude oil droplet on the 4 surfaces is shown in Figure 3a, with a comparison of the steady-state contact angles provided in Figure 3b. The general behavior is in good agreement with the Wenzel interpretation for roughened surfaces, where hydrophilic surfaces ($\theta < 90^\circ$) become increasingly hydrophilic with increased roughness, as described by $\cos \theta_w = R \cos \theta_y$, where R is the roughness ratio which is the total surface area to the projected surface area.

An observation following droplet dewetting was the presence of a “halo” pattern on the dewetted surfaces of P400 and P240 (Figure 3a, side view images). The droplet “halo” was more visible (greater contrast to the test substrate) on rougher surfaces, with the presence of daughter droplets becoming increasingly less visible on the P2500 surface and unobservable on the unpolished surface, thus confirming a higher frequency of micron-sized daughter droplets are formed on surfaces of increasing roughness. Further analysis of the P240 surface revealed a more prominent “halo” pattern toward the edge of the initial wetted perimeter, with the pattern becoming more diffuse further away from that boundary. A region within the “halo” was imaged by AFM and revealed features similar to a hemispherical cap (Figure 4a). Profile line analysis of one of these hemispherical caps was used to approximate its size, determining its major and minor axes to be ~ 15 and $\sim 10 \mu\text{m}$, respectively, and with a height of ~ 1.5

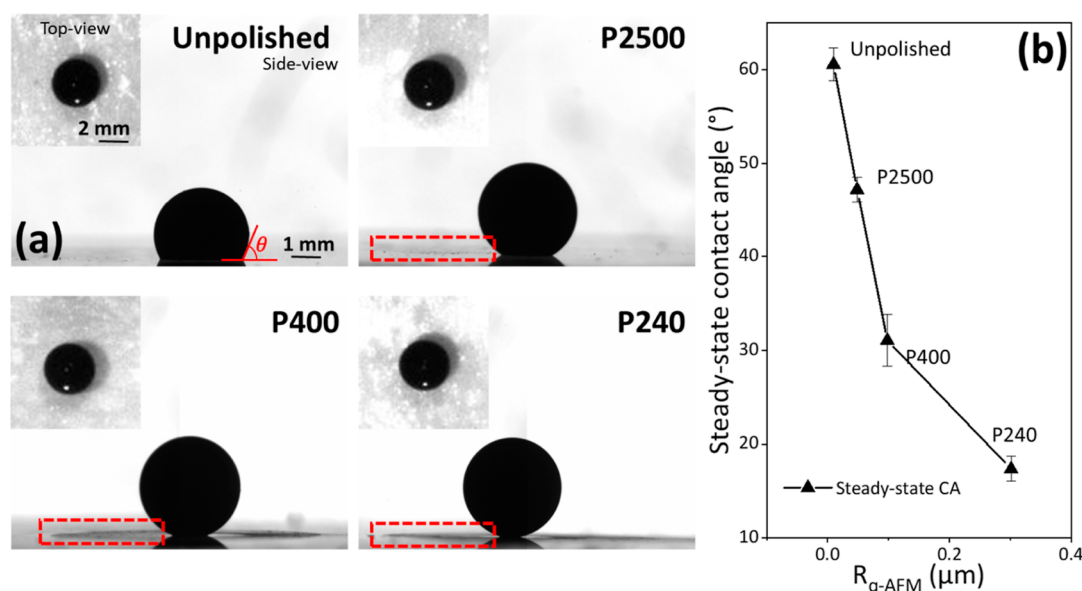


Figure 3. Side-view and top-view images of the oil droplet rest on the uncontaminated surface of varying roughness (a); the corresponding apparent steady-state contact angle (θ) measured through the aqueous phase (b). The steady-state contact angle is an average of the left and right contact angles, with the difference between the two contact angles within 2° . The oil retained on the surface in the dewetted region is highlighted by the dashed box.

μm . From the AFM image analysis, it is confirmed that these features are due to micron-sized oil droplets embedded within the roughened surface. Further evidence of these micron-sized droplets is provided in the Supporting Information (Figure S4a). It is thought that these micron-sized droplet are able to form because the oil fully wets the surface pits as it spreads on the surface in air.

It is thought that the formation of micron-sized droplets on roughened surfaces occurs because the deposited thin liquid-film in air Wenzel wets the surfaces. However, to verify the initial wetting condition, the approach of Zhang et al.³⁴ was followed, where the Gibbs free energy for Wenzel wetting is described by

$$G_W = [F(\theta_W)]^{-2/3} \times [2 - 2\cos\theta_W - r \times \sin^2\theta_W \times \cos\theta_Y] \quad (1)$$

where $\cos\theta_W = r \times \cos\theta_Y$, r is the roughness ratio which is the total surface area to the projected surface area, and θ_Y is the Young's angle of the oil droplet on the unpolished surface. And the Gibbs free energy for Cassie–Baxter wetting, which describes partial wetting caused by the thin liquid-film nonwetting into surface pits, is described by

$$G_{CB} = [F(\theta_{CB})]^{-2/3} \times [2 - 2\cos\theta_{CB} - \sin^2\theta_{CB} \times (-1 + f_s + f_s \times \cos\theta_Y)] \quad (2)$$

where $\cos\theta_{CB} = -1 + f_s \times (1 + \cos\theta_Y)$, and f_s is the fraction of the wetted surface. $F(\theta)$ for each wetted state is defined by $F(\theta_X) = 2 - 3\cos\theta_X + \cos^3\theta_X$, where θ_X is θ_W or θ_{CB} . The difference in energies of the two wetted states is then given by

$$\Delta G = G_{CB} - G_W \quad (3)$$

To determine the preferential wetted state, the parameter r was varied between 1 and 2 (with 1.137 being the maximum r value reported in Table 1) and f_s between 0.01 and 0.9. Figure S5 of the Supporting Information shows that for all conditions,

$G_{CB} > G_W$, and confirms that the initial wetted state of the oil droplet on the roughened surfaces in air is Wenzel wetting, hence when deposited in air the oil droplet wets into the surface pits.

With the oil film fully wetted on the roughened surface, once immersed in water the oil film spontaneously recedes, see Step 1 to Step 2 [Figure 4b(i)]. Step 2 shows the three-phase contact line at the incipient point of a surface pit (Point A_2). At A_2 the mobility of the contact line changes because of a change in the apparent contact angle, which at Point A_2 is given by, $\theta_{A_2} = \theta_{app} - \beta$, where θ_{app} is the apparent contact angle measured by the tensiometer [Figure 4b(i)], and β is the slope which is approximated to be $80.9 \pm 4.5^{\circ}$ from AFM imaging (Figure 4a).^{35,36} Taking θ_{app} to be the first measured contact angle during droplet dewetting, which is $\theta_{app} = 145.2 \pm 3.1^{\circ}$ (P240 surface), then θ_{A_2} is approximated to be 64.3° . The velocity of the contact line can be approximated according to the Cox–Voinov spreading law^{37,38}

$$U = \frac{\gamma_{OW}(\theta^3 - \theta_{eq}^3)}{9\mu \ln\left(\frac{R}{L}\right)} \quad (4)$$

where the γ_{OW} is the oil–water interfacial tension, θ is the dynamic contact angle, θ_{eq} is the equilibrium contact angle, μ is the viscosity of the oil droplet, R is the radius of the droplet and L is the microscopic cutoff length, taken to be $\sim 1 \text{ \AA}$.

With a difference in the apparent contact angles on the test substrate and at Point A_2 , the contact line velocity on the test substrate is 61 times larger than that of the local contact line velocity at Point A_2 ($\frac{U_{bulk}}{U_{A_2}} = 61$). As such, the three-phase contact line at Point A_2 appears almost pinned relative to the bulk movement of the oil droplet. This relative difference between the two contact line velocities leads to an increasing contact angle as the contact line moves from Point A_2 to Point A_4 , see Figure 4b lines 2, 3, and 4. As the three-phase contact line slowly migrates toward Point C in the surface pit, the

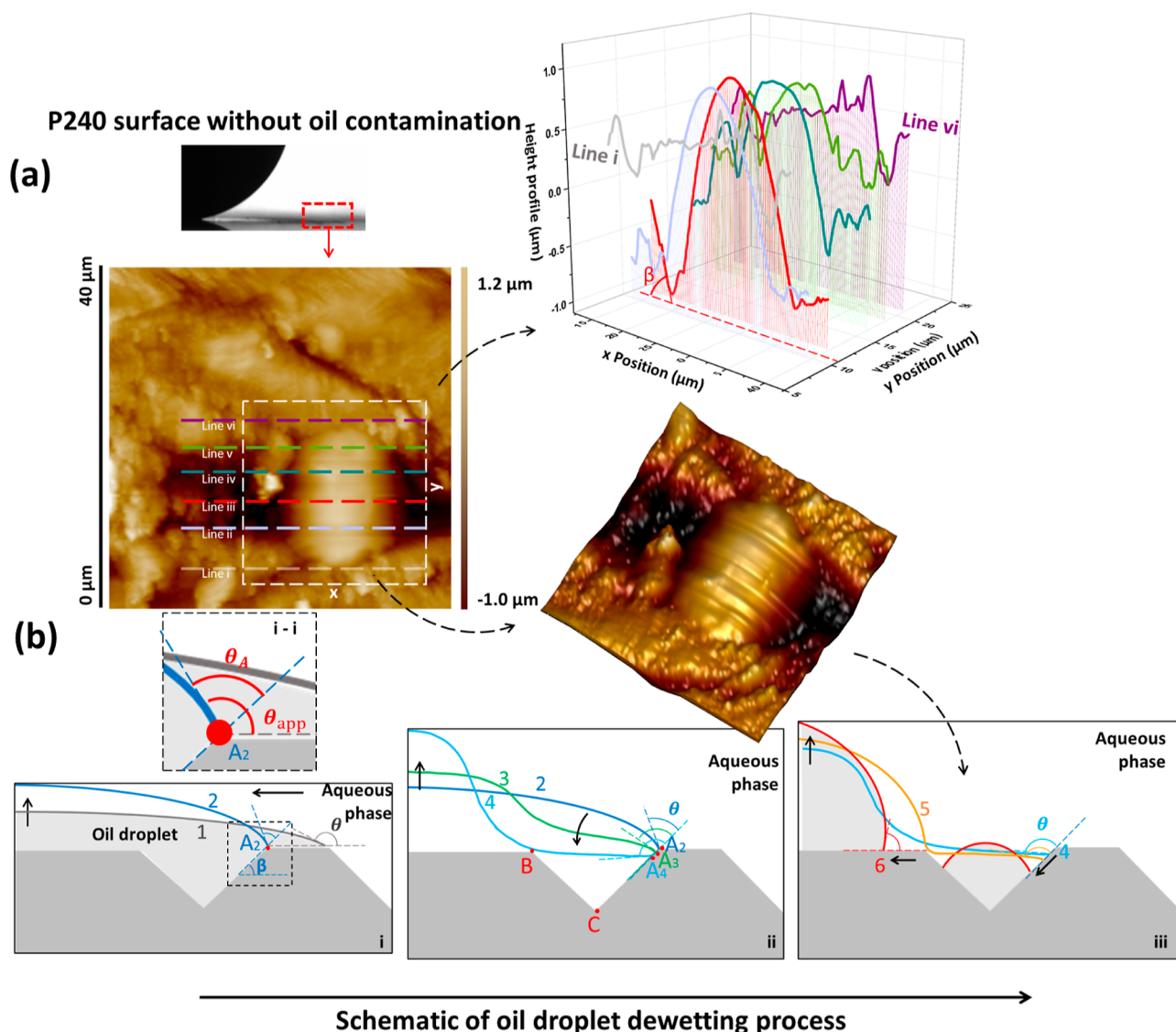


Figure 4. AFM imaged surface topography of P240 after oil droplet dewetting (a). The scanned area was chosen to identify the surface features within the apparent “halo” region as seen in Figure 3a. The white dashed box and its 3D-image highlights an area of interest that was analyzed by several line profiles: line (i) to line (vi). Additional line profiles perpendicular to the direction shown here are provided in Figure S4a of the Supporting Information. From the line profile analysis it is concluded that the “halo” region is many micron-sized droplets that are retained on the surface as the heavy crude oil film dewets. β is the inclination of the surface pit approximated from the line profiles [line (ii) to line (iv)]. Further AFM images on the same surface are provided in Figure S4b of the Supporting Information. The mechanism by which micron-sized daughter droplets are retained on the surface is schematically shown in (b), with each step further discussed.

thickness of the liquid film at Point B begins to thin. Eventually, and as a consequence of the attractive van der Waals forces (Hamaker constant of water–oil–solid is calculated to be -2.85×10^{-21} J), the liquid film is destabilized at a critical film thickness causing separation of a daughter droplet.^{12,37,39} The liquid in the surface pit continues to dewet and forms a spherical cap as shown in Figure 4a (measured) and 4b(iii). Clearly, the potential of forming daughter droplets depends on the relative motion of the localized contact line mobility to the bulk droplet mobility (velocity ratio), and the pathway length (size of surface pits) over which the velocity ratio is maintained. Hence, smaller and narrower pits are unlikely to form daughter droplets.

The above dewetting and film rupture process can be seen in the 3D visualizations of the numerical simulations in Figure 5 where the simulated surface is only roughened but chemically

homogeneous. The initial configuration corresponds to an oil droplet at equilibrium on a dry substrate, with a contact angle of $\sim 155^\circ$ measured through the surrounding air. To mimic what happens when the oil droplet is immersed in water, at $t = 0$, the substrate wettability is set to $\eta = 0.3$, which corresponds to a contact angle of $\sim 60^\circ$ (measured through the water). This triggers a rapid retraction of the contact line toward the oil phase, and advancement of the water phase from right to left. A short distance behind the initial contact line is a distinct surface pit, larger than the small pits covering the whole solid surface. It is deeper in its center and shallower to the sides and is intended as an idealized representation of the part of the substrate shown in the AFM images in Figure 4.

The contact line is able to move rapidly and recede cleanly over the small pits and shallow parts of the main pit, but as noted in Figure 4, it becomes pinned on the relatively sharp

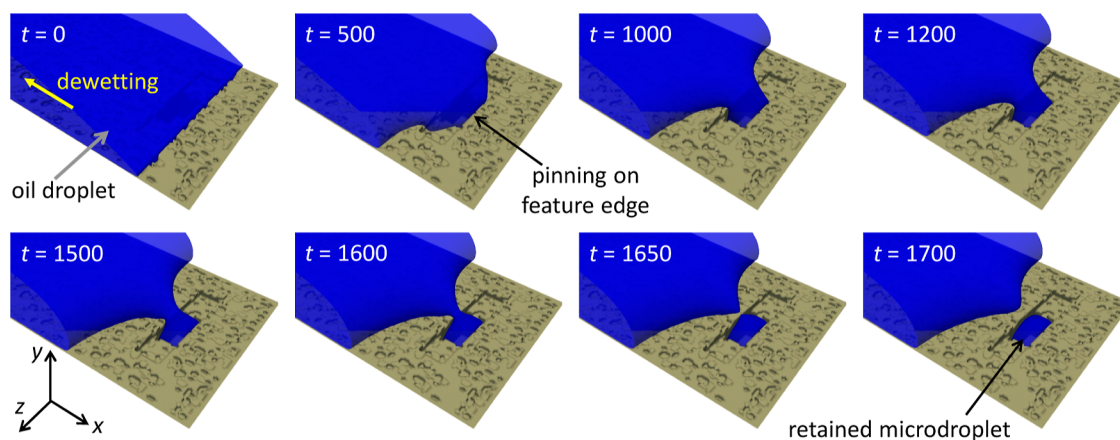


Figure 5. Lattice Boltzmann simulations of dewetting on a chemically homogeneous but topographically nonuniform surface. The oil droplet is modeled as a segment of an infinitely long bead of liquid, with an initial contact angle of 155° (through the surrounding aqueous phase). The substrate has a uniform wettability $\eta = 0.3$, corresponding to a (water) contact angle of approximately 60° , leading to spontaneous dewetting. A distinct surface pit lies behind the initial contact line and features a shallow outer region and deeper central pit. Contact-line pinning on this feature slows local dewetting and ultimately leads to separation and microdroplet formation. Time is indicated as the number of (constant) time steps of the simulation.

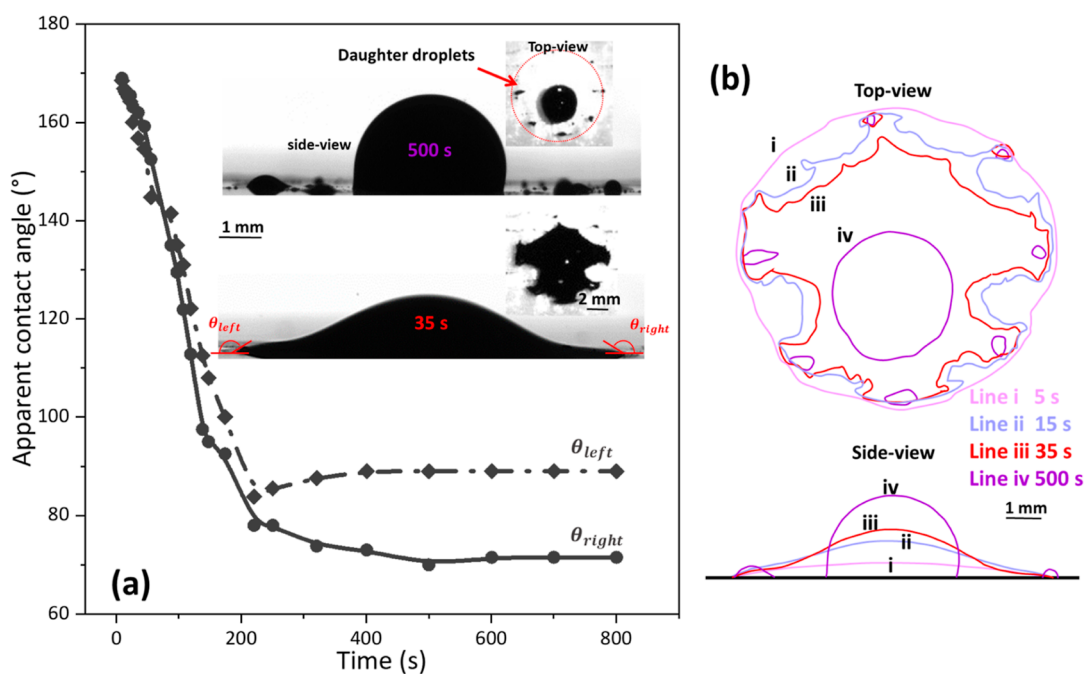


Figure 6. Receding dynamics of a thin oil film on an unpolished oil contaminated surface (a). Contact angles are measured through the aqueous phase with both the left and right contact angles reported due to the nonuniformity of the droplet perimeter during dewetting (b). Line (i) to line (iv) in (b) represent the line profiles of the droplet perimeter at different time intervals.

edge of the central part of the pit, unable to move down the interior of the pit because of the Gibbs criterion. The continued recession of the contact line either side of the pit results in the formation of a neck and the ultimate rupture and detachment of a microdroplet that remains within the pit. Postrupture, the highly curved section of the contact line accelerates to catch up with the rest of the contact line. Since the wettability of the simulated solid is uniform everywhere, the observed behavior is entirely due to geometrical rather than chemical heterogeneity.

3.3. Droplet Dewetting on Smooth and Roughened Surfaces (with Oil Contamination). Figure 6a shows the dewetting dynamics of a heavy crude oil droplet initially deposited on an unpolished oil contaminated surface. With a

steady-state contact angle of, $\theta = 88.7 \pm 13.1^\circ$ (averaged left and right contact angles), the change in the Gibbs free energy is -0.52 mN/m, confirming again that the oil film will spontaneously dewet when immersed in water. The difference between the left and right contact angles ($\sim 20^\circ$) suggests that the surface is nonuniform, with localized surface properties dictating the behavior of the three-phase contact line, see Figure 6b. Our previous study confirmed that the method used to contaminate the surfaces produces smooth but chemically heterogeneous surfaces due to the asphaltene deposits (hydrophobic patches),¹² see also Figure 2b(I). Those hydrophobic deposits hinder the mobility of the local three-phase contact line which leads to localized differences in the relative velocity of the contact line around the droplet

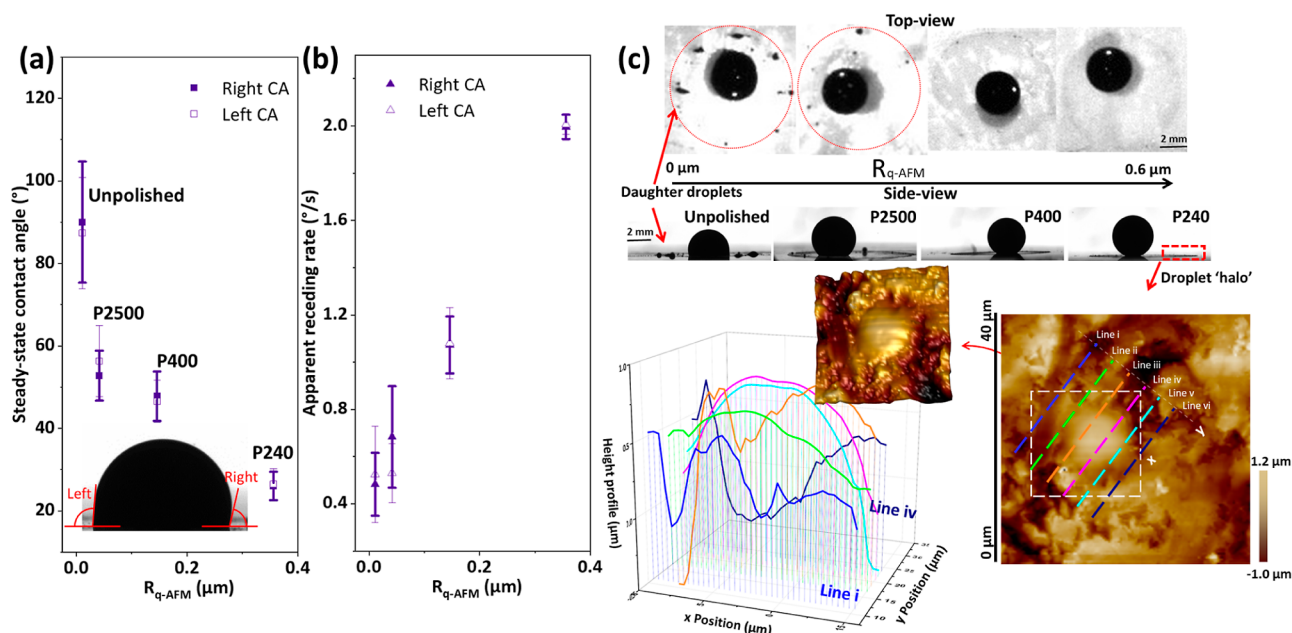


Figure 7. Apparent steady-state contact angles of oil droplets on oil contaminated roughened surfaces (a), with the inset image showing the left and right contact angles on the P240 oil contaminated surface. Apparent initial droplet receding rates on the same surfaces (b). Side and top views of the receded droplets on surfaces of increasing roughness: unpolished \rightarrow P240 (c). AFM image of the P240 surface with several line profiles [line (i) to line (iv)] confirming the retention of micron-sized oil droplets on the roughened surface. Additional line profiles perpendicular to the direction shown here are provided in Figure S4a of the [Supporting Information](#). Further AFM images on the same surface are provided in Figure S4c of the [Supporting Information](#).

perimeter. We used the lattice Boltzmann method to show that the formation of daughter droplets depends on the patch size and receding angle on the patch. For smaller hydrophobic patches, the critical receding angle to form daughter droplets is larger than that on larger hydrophobic patches, as a greater disparity in receding dynamics, on and off the hydrophobic patch, is needed to establish a liquid neck that eventually collapses. However, the droplets formed on these surfaces (Figure 6a) tend to be larger than those formed on roughened surfaces, likely due to smaller differences in the localized receding contact angle compared to that on roughened surfaces, see previous discussion. Further discussion on the mechanism elucidated by LBM simulations is provided in our previous publication, see Jiang et al.¹²

Changes in the steady-state contact angles on oil contaminated surfaces of varying roughness (Figure 7a) are consistent with those seen without contamination (Figure 3b), although the contact angle values are slightly higher due to the distribution of hydrophobic patches on the hydrophilic surface. Furthermore, the apparent receding rate increases with higher surface roughness (Figure 7b) as the surface energy becomes more unfavorable, see Figure 7a.²⁹ For oil contaminated unpolished surfaces, discrete millimeter-sized daughter droplets are found to be randomly distributed in the region of the initial wetted boundary (Figure 7c, l.h.s. image). As previously discussed, differences in the relative velocities of the local contact lines on adjacent hydrophilic and hydrophobic patches can lead to forming large daughter droplets. However, for rougher surfaces those large daughter droplets disappear, although residual oil is still retained on the dewetted surface but as smaller micron-sized droplets, see Figure 7c (r.h.s. image) and the AFM line profile analysis which confirms micron-sized droplet to be buried within the roughened surface. The top view images in Figure 7c reveal a dense and

uniform distribution of these micron-sized droplets on the roughest oil contaminated surface, such that the dewetted region appears as a “halo” around the primary oil droplet.

The transition between the dominant surface characteristic, either chemical or physical, and the influence of each on forming daughter droplets changes with increasing surface roughness, see Figure 8. Only on unpolished chemically

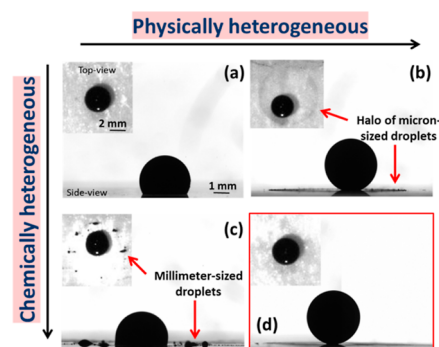


Figure 8. Phase-map of daughter droplets formed on physically and chemically heterogeneous surfaces. Side and top view images of dewetted oil droplets at steady-state showing the effects of physical and chemical heterogeneity. Surface properties include: unpolished and uncontaminated surface (a); P240 surface without oil contamination (b); unpolished oil contaminated surface (c); P240 surface with oil contamination (d).

heterogeneous surfaces (Figure 8c) are discrete millimeter-sized daughter droplets formed. While on roughened surfaces (Figure 8b,d) and independent of chemical heterogeneity, a dense pattern of micron-sized droplets remains as the primary droplet recedes. Daughter droplets form due to variations in the local contact line mobility around the droplet perimeter,

which for unpolished chemically heterogeneous surfaces is caused by the chemical patch changing the droplet-substrate adhesion and modifying the critical receding angle (θ_c).¹² With the receding contact angle being similar on both the unpolished and roughened (P240) chemically heterogeneous surfaces (Figure S1c) the contribution from surface adhesion alone cannot describe the formation of both millimeter and micron-sized droplets. The formation of micron-sized droplets is attributed to the changing apparent contact angle of the contact line within surface pits, slowing its migration relative to the bulk fluid. The reduced effect of chemical heterogeneity on roughened surfaces and the absence of millimeter size droplets is likely attributed to the small size of the chemical patch, with the patch size being more disrupted by the surface asperities.

4. CONCLUSIONS

Droplet dewetting on surfaces where both chemical and physical heterogeneities coexist is rarely studied but is often encountered in practice.^{40–42} On smooth surfaces with chemical heterogeneity we have shown large daughter droplets form as an oil film recedes.¹² These droplets form due to the uneven motion of the local contact line, with the contact line of the oil droplet moving slower on hydrophobic patches relative to that on the underlying hydrophilic substrate. Although the deposited hydrophobic patches (chemical modification) slightly roughen the surface (nanoscale roughness), its effect on the dewetting behavior was found to be negligible. Those same surfaces have been considered in the current study, but the surfaces were physically roughened so the effect of surface roughness with and without chemical modification can be better understood.

For roughened uncontaminated surfaces, micron-sized droplets were formed as the oil droplet receded, with those droplets appearing as a “halo” around the dewetted droplet. AFM imaging revealed those micron-sized droplets to be trapped in the surface pits. Those droplets formed because of differences in the local contact line mobility which becomes significantly retarded in a surface pit due to the higher apparent contact angle relative to the direction of droplet dewetting. This leads to drainage of the thin liquid film over a surface pit and eventual rupture, leaving behind a micron-sized droplet. The same residual pattern of droplets was also seen on the chemically contaminated surfaces, but only for the roughened (microscale) surfaces. The study showed that for rough surfaces, droplet dewetting behavior is strongly influenced by the physical roughness and less so the chemical heterogeneity, although the latter does become more important on smoother (nanoscale) surfaces where the size of discrete chemical heterogeneities (surface patches) can be much larger as they are undisturbed by the physical roughness.

The importance of thin liquid-film dynamics on surfaces impacts a range of processes from cleaning to oil recovery.^{43–45} Understanding how surface heterogeneities contribute to contact line dynamics of a receding thin liquid film, and being able to predict different behaviors, is only possible when studying thin film dynamics at the micron length scales. These new insights are beginning to provide an understanding as to how these complex systems behave, with impact potentially broader than the traditional engineering problems, for example, understanding how viral aerosols are retained on surfaces.^{46,47}

■ ASSOCIATED CONTENT

Supporting Information

The Supporting Information is available free of charge at <https://pubs.acs.org/doi/10.1021/acs.energyfuels.4c02756>.

The Supporting Information contains additional experimental details and data. The method used to measure the receding contact angles and associated data are provided in Figure S1. Confocal light scanning microscopy images of the prepared surfaces are provided in Figure S2, and experimental repeats of the dewetting studies on those surfaces are shown in Figure S3. Additional regions scanned by AFM are also included showing more entrapped micron-sized oil droplets in surface pits (Figure S4). Figure S5 provides an assessment of the free energy change (ΔG) as a function of r and f_s (PDF)

■ AUTHOR INFORMATION

Corresponding Authors

David Harbottle – School of Chemical and Process Engineering, University of Leeds, LS2 9JT Leeds, U.K.; orcid.org/0000-0002-0169-517X; Email: d.harbottle@leeds.ac.uk

Mark C. T. Wilson – School of Mechanical Engineering, University of Leeds, LS2 9JT Leeds, U.K.; orcid.org/0000-0002-1058-2003; Email: M.Wilson@leeds.ac.uk

Authors

Jiatong Jiang – School of Petroleum, China University of Petroleum-Beijing at Karamay, 834099 Karamay, China; School of Chemical and Process Engineering, University of Leeds, LS2 9JT Leeds, U.K.

Suparit Tangparitkul – Department of Mining and Petroleum Engineering, Chiang Mai University, 50200 Chiang Mai, Thailand; orcid.org/0000-0003-4316-3304

Complete contact information is available at: <https://pubs.acs.org/10.1021/acs.energyfuels.4c02756>

Notes

The authors declare no competing financial interest.

■ ACKNOWLEDGMENTS

J.J. thanks the China Scholarship Council (scholarship no. 201906440066), the MOE Key Laboratory of Petroleum Engineering (China University of Petroleum), and the Science Foundation of China University of Petroleum (no. ZX20240159; no. 2462024QZDX004) for supporting this research. S.T. acknowledges Chiang Mai University for supporting the collaboration with the University of Leeds. The authors would like to acknowledge the experimental assistance of Rob Simpson (School of Chemical and Process Engineering, University of Leeds) who provided guidance on using the confocal laser scanning microscope.

■ REFERENCES

- Geyer, F.; D'Acunzi, M.; Sharifi-aghili, A.; Saal, A.; Gao, N.; Kaltbeitzel, A.; Slood, T.; Berger, R.; Butt, H.; Vollmer, D. When and How Self-Cleaning of Superhydrophobic Surfaces Works. *Sci. Adv.* **2020**, *6* (3), 1–12.
- Jeong, C.; Lee, J.; Sheppard, K.; Choi, C. Air-Impregnated Nanoporous Anodic Aluminum Oxide Layers for Enhancing the

- Corrosion Resistance of Aluminum. *Langmuir* **2015**, *31* (40), 11040–11050.
- (3) Lin, F.; He, L.; Hou, J.; Masliyah, J.; Xu, Z. Role of Ethyl Cellulose in Bitumen Extraction from Oil Sands Ores Using an Aqueous – Nonaqueous Hybrid Process. *Energy Fuels* **2016**, *30* (1), 121–129.
- (4) Pan, B.; Clarkson, C. R.; Atwa, M.; Debuhr, C.; Ghanizadeh, A.; Birss, V. I. Wetting Dynamics of Nanoliter Water Droplets in Nanoporous Media. *J. Colloid Interface Sci.* **2021**, *589*, 411–423.
- (5) Tangparitkul, S.; Hodges, C. S.; Ballard, D. A.; Niu, Z.; Pradilla, D.; Charpentier, T. V. J.; Xu, Z.; Harbottle, D. Dewetting Dynamics of Heavy Crude Oil Droplet in Low-Salinity Fluids at Elevated Pressures and Temperatures. *J. Colloid Interface Sci.* **2021**, *596*, 420–430.
- (6) Wilson, M. C. T.; Kubiak, K. J. Simulation of Drops on Surfaces. *Fundamentals of Inkjet Printing*; John Wiley & Sons, 2016; pp 281–312.
- (7) Dent, F. J.; Harbottle, D.; Warren, N. J.; Khodaparast, S. Exploiting Breath Figure Reversibility for In-Situ Pattern Modulation and Hierarchical Design. *Soft Matter* **2023**, *19*, 2737–2744.
- (8) Dent, F. J.; Harbottle, D.; Warren, N. J.; Khodaparast, S. Temporally Arrested Breath Figure. *ACS Appl. Mater. Interfaces* **2022**, *14* (23), 27435–27443.
- (9) Sykes, T. C.; Harbottle, D.; Khatir, Z.; Thompson, H. M.; Wilson, M. C. T. Substrate Wettability Influences Internal Jet Formation and Mixing during Droplet Coalescence. *Langmuir* **2020**, *36* (32), 9596–9607.
- (10) Sykes, T. C.; Castrejón-Pita, A. A.; Castrejón-Pita, J. R.; Harbottle, D.; Khatir, Z.; Thompson, H. M.; Wilson, M. C. T. Surface Jets and Internal Mixing during the Coalescence of Impacting and Sessile Droplets. *Phys. Rev. Fluids* **2020**, *5* (2), 023602.
- (11) James, E.; Tangparitkul, S.; Brooker, A.; Amador, C.; Graydon, A.; Vaccaro, M.; Cayre, O. J.; Hunter, T. N.; Harbottle, D. Accelerated Spreading of Inviscid Droplets Prompted by the Yielding of Strongly Elastic Interfacial Films. *Colloids Surf., A* **2018**, *554* (February), 326–333.
- (12) Jiang, J.; Jackson, F.; Tangparitkul, S.; Wilson, M. C. T.; Harbottle, D. Discontinuous Dewetting Dynamics of Highly Viscous Droplets on Chemically Heterogeneous Substrates. *J. Colloid Interface Sci.* **2023**, *629*, 345–356.
- (13) Podgorski, T.; Flesselles, J. M.; Limat, L. Corners, Cusps, and Pearls in Running Drops. *Phys. Rev. Lett.* **2001**, *87* (3), 036102–361024.
- (14) Wenzel, R. N. Resistance of solid surfaces to wetting by water. *Ind. Eng. Chem.* **1936**, *28* (8), 988–994.
- (15) Drelich, J. W. Contact Angles: From Past Mistakes to New Developments through Liquid-Solid Adhesion Measurements. *Adv. Colloid Interface Sci.* **2019**, *267*, 1–14.
- (16) Kubiak, K. J.; Wilson, M. C. T.; Mathia, T. G.; Carval, P. Wettability versus Roughness of Engineering Surfaces. *Wear* **2011**, *271* (3–4), 523–528.
- (17) Wang, D.; Zhu, Z.; Yang, B.; Yin, W.; Drelich, J. W. Nano-Scaled Roughness Effect on Air Bubble-Hydrophilic Surface Adhesive Strength. *Colloids Surf., A* **2020**, *603* (April), 125228.
- (18) Hu, X.; Wang, Z.; Hwang, D. J.; Colosqui, C. E.; Cubaud, T. Viscous Liquid-Liquid Wetting and Dewetting of Textured Surfaces. *Soft Matter* **2021**, *17* (4), 879–886.
- (19) Cassie, A. B. D. Contact Angles. *Discuss. Faraday Soc.* **1948**, *3*, 11–16.
- (20) Iwamatsu, M. The Validity of Cassie's Law: A Simple Exercise Using a Simplified Model. *J. Colloid Interface Sci.* **2006**, *294* (1), 176–181.
- (21) Chang, B.; Kivinen, O.; Pini, I.; Levkin, P. A.; Ras, R. H. A.; Zhou, Q. Nanoliter Deposition on Star-Shaped Hydrophilic–Superhydrophobic Patterned Surfaces. *Soft Matter* **2018**, *14*, 7500–7506.
- (22) Liu, T. L.; Chen, Z.; Kim, C. J. A Dynamic Cassie-Baxter Model. *Soft Matter* **2015**, *11* (8), 1589–1596.
- (23) Cassie, A. B. D.; Baxter, S. Wettability of Porous Surfaces. *Trans. Faraday Soc.* **1944**, *40* (5), 546–551.
- (24) Jiang, Y.; Choi, C. H. Droplet Retention on Superhydrophobic Surfaces: A Critical Review. *Adv. Mater. Interfaces* **2021**, *8* (2), 2001205.
- (25) Jiang, Y.; Xu, W.; Sarshar, M. A.; Choi, C. H. Generalized Models for Advancing and Receding Contact Angles of Fakir Droplets on Pillared and Pored Surfaces. *J. Colloid Interface Sci.* **2019**, *552*, 359–371.
- (26) Sbragaglia, M.; Peters, A. M.; Pirat, C.; Borkent, B. M.; Lammertink, R. G. H.; Wessling, M.; Lohse, D. Spontaneous Breakdown of Superhydrophobicity. *Phys. Rev. Lett.* **2007**, *99* (15), 156001–156004.
- (27) Hou, B.; Wu, C.; Li, X.; Huang, J.; Chen, M. Contact Line-Based Model for the Cassie-Wenzel Transition of a Sessile Droplet on the Hydrophobic Micropillar-Structured Surfaces. *Appl. Surf. Sci.* **2021**, *542* (November 2020), 148611–148612.
- (28) Murakami, D.; Jinnai, H.; Takahara, A. Wetting Transition from the Cassie-Baxter State to the Wenzel State on Textured Polymer Surfaces. *Langmuir* **2014**, *30* (8), 2061–2067.
- (29) Tangparitkul, S.; Charpentier, T.; Pradilla, D.; Harbottle, D. Interfacial and Colloidal Forces Governing Oil Droplet Displacement: Implications for Enhanced Oil Recovery. *Colloids Interfaces* **2018**, *2* (3), 30.
- (30) Tangparitkul, S.; Jiang, J.; Jeraal, M.; Charpentier, T. V. J.; Harbottle, D. Competitive Adsorption of Interfacially Active Nanoparticles and Anionic Surfactant at the Crude Oil – Water Interface. *Langmuir* **2023**, *39* (7), 2483–2490.
- (31) Chen, L.; Yu, J.; Wang, H. Convex Nanobending at a Moving Contact Line: The Missing Mesoscopic Link in Dynamic Wetting. *ACS Nano* **2014**, *8* (11), 11493–11498.
- (32) Al-Ghaithi, K. H. A.; Harlen, O. G.; Kapur, N.; Wilson, M. C. T. Morphologies and Dynamics of Micro-Droplet Impact onto an Idealised Scratch. *J. Fluid Mech.* **2021**, *925*, A23–A34.
- (33) Castrejón-Pita, J. R.; Kubiak, K. J.; Castrejón-Pita, A. A.; Wilson, M. C. T.; Hutchings, I. M. Mixing and Internal Dynamics of Droplets Impacting and Coalescing on a Solid Surface. *Phys. Rev. E: Stat., Nonlinear, Soft Matter Phys.* **2013**, *88* (2), 023023.
- (34) Zhang, Y.; Klittich, M. R.; Gao, M.; Dhinojwala, A. Delaying Frost Formation by Controlling Surface Chemistry of Carbon Nanotube-Coated Steel Surfaces. *ACS Appl. Mater. Interfaces* **2017**, *9* (7), 6512–6519.
- (35) Deng, Y.; Xu, L.; Lu, H.; Wang, H.; Shi, Y. Direct Measurement of the Contact Angle of Water Droplet on Quartz in a Reservoir Rock with Atomic Force Microscopy. *Chem. Eng. Sci.* **2018**, *177*, 445–454.
- (36) Savulescu, G. C.; Rücker, M.; Scanziani, A.; Pini, R.; Georgiadis, A.; Luckham, P. F. Atomic Force Microscopy for the Characterisation of Pinning Effects of Seawater Micro-Droplets in n-Decane on a Calcite Surface. *J. Colloid Interface Sci.* **2021**, *592*, 397–404.
- (37) Yu, H.; Kant, P.; Dyett, B.; Lohse, D.; Zhang, X. Splitting Droplets through Coalescence of Two Different Three-Phase Contact Lines. *Soft Matter* **2019**, *15* (30), 6055–6061.
- (38) Yang, H.; Zeng, B.; Lu, Q.; Xing, Y.; Gui, X.; Cao, Y.; Xu, B. B.; Zhang, X. Shaping a Surface Microdroplet by Marangoni Forces along a Moving Contact Line of Four Immiscible Phases. *Adv. Mater. Interfaces* **2024**, *11* (14), 1–9.
- (39) Vrij, A.; Overbeek, J. T. G. Rupture of Thin Liquid Films Due to Spontaneous Fluctuations in Thickness. *J. Am. Chem. Soc.* **1968**, *90*, 3074–3078.
- (40) Li, W.; Lu, J.; Tryggvason, G.; Zhang, Y. Numerical study of droplet motion on discontinuous wetting gradient surface with rough strip. *Phys. Fluids* **2021**, *33* (1), 012111.
- (41) Snels, L.; Mostofi, N.; Soete, J.; Maes, A.; Antonini, C.; Wevers, M.; Maitra, T.; Seveno, D. Internal and Interfacial Microstructure Characterization of Ice Droplets on Surfaces by X-Ray Computed Tomography. *J. Colloid Interface Sci.* **2023**, *637*, 500–512.

(42) Guo, Z.; Liu, J.; Li, Q.; Lei, Z.; Zhou, Y.; Hu, P. Effect of Surface Heterogeneities on Interactions between Air Bubbles and Heterogeneous Surfaces. *Langmuir* **2022**, *38* (32), 9908–9916.

(43) Yang, S.; Chen, L.; Wang, C.; Rana, M.; Ma, P. Surface Roughness Induced Superhydrophobicity of Graphene Foam for Oil-Water Separation. *J. Colloid Interface Sci.* **2017**, *508*, 254–262.

(44) Rücker, M.; Bartels, W.; Garfi, G.; Shams, M.; Bultreys, T.; Boone, M.; Pieterse, S.; Maitland, G.; Krevor, S.; Cnudde, V.; et al. Relationship between Wetting and Capillary Pressure in a Crude Oil/Brine/Rock System: From Nano-Scale to Core-Scale. *J. Colloid Interface Sci.* **2020**, *562*, 159–169.

(45) Cao, Y.; Salvini, A.; Camaiti, M. One-Step Fabrication of Robust and Durable Superamphiphobic, Self-Cleaning Surface for Outdoor and in Situ Application on Building Substrates. *J. Colloid Interface Sci.* **2021**, *591*, 239–252.

(46) Mallakpour, S.; Azadi, E.; Mustansar, C. Fabrication of Air Filters with Advanced Filtration Performance for Removal of Viral Aerosols and Control the Spread of COVID-19. *Adv. Colloid Interface Sci.* **2022**, *303* (March), 102653.

(47) Huang, Q.; Wang, W.; Vikesland, P. J. Implications of the Coffee-Ring Effect on Virus Infectivity. *Langmuir* **2021**, *37* (38), 11260–11268.